Impact of vertical mixing parameterizations on internal gravity wave spectra in regional ocean models

Ritabrata Thakur[1,1], Brian K. Arbic[2,2], Dimitris Menemenlis[3,3], Kayhan Momeni[4,4], Yulin Pan[1,1], W Richard Peltier[5,5], Joseph Skitka[1,1], Matthew H Alford[6,6], and Yuchen Ma[4,4]

[1]University of Michigan Ann Arbor
[2]University of Michigan-Ann Arbor
[3]Jet Propulsion Laboratory, California Institute of Technology
[4]University of Toronto
[5]Department of Physics, University of Toronto
[6]Scripps Institution of Oceanography

November 30, 2022

Abstract

We present improvements in the vertical wavenumber spectrum of the internal gravity wave continuum in high-resolution regional ocean simulations. We focus on model sensitivities to mixing parameters and comparisons to McLane moored profiler observations in a Pacific region near the Hawaiian Ridge, which features strong semidiurnal tidal beams. In these simulations, the modeled continuum exhibits high sensitivity to the background mixing components of the K-Profile Parameterization (KPP) vertical mixing scheme. Without the KPP background mixing, stronger vertical gradients in velocity are sustained in the simulations and the modeled kinetic energy and shear spectral slopes are significantly closer to the observations. The improved representation of internal wave dynamics in these simulations makes them suitable for improving ocean mixing estimates and for the interpretation of satellite missions such as the Surface Water and Ocean Topography (SWOT) mission.

Impact of vertical mixing parameterizations on internal gravity wave spectra in regional ocean models

Ritabrata Thakur[1], Brian K. Arbic[1], Dimitris Menemenlis[2], Kayhan Momeni[3], Yulin Pan[4], W. R. Peltier[3], Joseph Skitka[1], Matthew H. Alford[5], Yuchen Ma[3]

[1]Department of Earth and Environmental Sciences, University of Michigan, Ann Arbor, MI, USA
[2]Jet Propulsion Laboratory, California Institute of Technology, Pasadena, CA, USA
[3]Department of Physics, University of Toronto, Toronto, Canada
[4]Department of Naval Architecture and Marine Engineering, University of Michigan, Ann Arbor, MI, USA
[5]Scripps Institution of Oceanography, University of California San Diego, La Jolla, CA, USA

Key Points:

- Regional ocean simulations are ideal for examining sensitivity of IGW spectra to model mixing parameters
- Turning off the KPP background yields more realistic IGW vertical structure in high-resolution regional models
- IGW spectra are most correctly estimated in models away from tidal generation sites and lateral boundaries

Corresponding author: Ritabrata Thakur, `ritabrata90official@gmail.com`

Abstract

We present improvements in the modeling of the vertical wavenumber spectrum of the internal gravity wave continuum in high-resolution regional ocean simulations. We focus on model sensitivities to mixing parameters and comparisons to McLane moored profiler observations in a Pacific region near the Hawaiian Ridge, which features strong semidiurnal tidal beams. In these simulations, the modeled continuum exhibits high sensitivity to the background mixing components of the K-Profile Parameterization (KPP) vertical mixing scheme. Without the KPP background mixing, stronger vertical gradients in velocity are sustained in the simulations and the modeled kinetic energy and shear spectral slopes are significantly closer to the observations. The improved representation of internal wave dynamics in these simulations makes them suitable for improving ocean mixing estimates and for the interpretation of satellite missions such as the Surface Water and Ocean Topography (SWOT) mission.

Keywords: internal gravity waves, vertical wavenumber spectra, MITgcm, KPP mixing parameterization

Plain Language Summary

Internal waves exist in the ocean interior due to differences in fluid densities. Breaking internal waves cause mixing, which has important effects on ocean temperatures and nutrients. Interactions between internal tides generated by tidal flow over bathymetric features and near-inertial waves generated by wind yield a spectrum of internal waves at many frequencies. Here, we compare the internal wave spectrum in high-resolution numerical simulations of a region in the North Pacific with observations from moored instruments. We study the effects of the background mixing components of the widely used K-Profile Parameterization (KPP) vertical mixing scheme on the vertical structure of the internal wave field. The KPP background parameterizes the mixing action of internal waves, which is not resolved in coarser-resolution global ocean models. In our high-resolution simulations, the internal wave field is highly active, and the KPP background components turn out to be mostly redundant in this setting. The modeled internal wave field lies closer to observations when we turn off the KPP background. Improved internal wave representation in ocean models can play an important role in the accurate representation of internal-wave-driven mixing in ocean simulations and interpretation of internal wave signatures from the Surface Water and Ocean Topography mission.

1 Introduction

This paper focuses on the vertical structure of the internal gravity wave (IGW; also simply "internal wave", or IW) spectrum in regional ocean models. At tidal frequencies, IWs are called internal tides (ITs) and are primarily generated by large-scale barotropic tides moving over topography (e.g., Baines, 1982; Bell, 1975). High-frequency changes in wind forcing generate near-inertial (NI) IWs at the ocean surface, having frequencies close to the Coriolis frequency (reviewed in Alford et al. (2016)). The high-frequency IW continuum is thought to arise from nonlinear interactions of ITs, NI motions, and the IW continuum, and also due to local exchanges between ITs and low-frequency motions (e.g., van Haren, 2016; Barkan et al., 2017). The variable distribution of IWs and IW-generated turbulence (Kunze, 2017b) inspire continued interest due to its importance in vertical temperature redistribution (e.g., as in the Arctic; D'Asaro & Morison, 1992) and the global overturning circulation (Munk & Wunsch, 1998; Wunsch & Ferrari, 2004; Kunze, 2017a), their role in the enhancement of primary productivity by redistribution of nutrients (X. Pan et al., 2012), and important feedback to climate (MacKinnon et al., 2017; Whalen et al., 2020).

Global high-resolution ocean general circulation models with simultaneous tidal and atmospheric forcing carry a partially-resolved IW continuum (Müller et al., 2015; Rocha, Chereskin, et al., 2016; Arbic et al., 2018). These global models fall short of representing the real ocean due to a lack of resolution and/or insufficient parameterization of unresolved sub-grid scale physical processes such as IW breaking. Regional ocean models have been shown to display improved IW spectra over those in the global models when run at higher horizontal and vertical resolutions, as long as the lateral boundary forcing includes remotely-generated IWs from a global IW model (Mazloff et al., 2020; Nelson et al., 2020). Such remotely-forced regional models run over short periods are relatively affordable computationally and can be used to study the sensitivity of the IW continuum due to changes in model parameters.

Here, we study high-resolution regional simulations of the Massachusetts Institute of Technology general circulation model (MITgcm; Marshall et al., 1997) forced at their lateral boundaries by a global MITgcm simulation, named LLC4320, that has been widely studied (e.g., Rocha, Chereskin, et al., 2016; Rocha, Gille, et al., 2016; Savage et al., 2017; Su et al., 2018). Regional simulations forced by LLC4320 have recently been used to study the sensitivity of the IW continuum to model resolution (Nelson et al., 2020) and to understand the mechanisms involved in the formation of the continuum (Y. Pan et al., 2020). In this paper, we study the sensitivity of the IW vertical wavenumber spectra to the cumulative effect of the background vertical viscosity and diffusivity components of the K-Profile Parameterization (KPP; Large et al., 1994).

In our regional simulations, we focus on a region in the Pacific Ocean northward of Hawaii (Fig 1). This region has heightened semi-diurnal (M_2) ITs that propagate northward from the islands (Fig 1 (b)) and undergo parametric subharmonic instability (PSI) at the critical latitude of 28.8° N, where the local inertial frequency is half of the M_2 tidal frequency. In contrast with the shear field at other latitudes in this region, marginally-stable shear layers with elevated NI energy generated via PSI of the IT are observed at 28.8° N (Alford et al., 2007). The northward-propagating ITs also interact with southbound IT beams from the Aleutian Ridge (not in the simulation domain), generating a complex IT field (e.g., Zhao et al. (2010); Alford et al. (2019)). We present improvements in the modeled IW vertical structure in these regional simulations by comparing them to observational data obtained using McLane moored profilers (Doherty et al., 1999; Morrison et al., 2001) (Fig 1 (b)). We find that the vertical wavenumber spectra of KE and shear shows appreciable improvement when the KPP background mixing is turned off. We also discuss the characteristics of shear spectra across different frequency bands in simulations with the KPP background turned off. The model captures the vertical structure of the NI band, which is an important component of the total shear, whereas the primary deficiency of the model relative to observations lies in the high-frequency (supertidal) IW continuum. We further study the sensitivity of modeled strain spectra to the KPP background components and quantify spectral improvements with model vertical resolution.

2 Data and methods

2.1 MITgcm model

Using the MITgcm, we simulate a 6° × 8° region north of the French Frigate Shoals, Hawaii, in the Pacific Ocean as shown in Fig 1. We study a suite of regional ocean simulations with 109, 153, and 264 vertical levels and a constant horizontal grid spacing of 1/48° (∼2km in the simulation domain). The vertical level thicknesses of our regional sim-

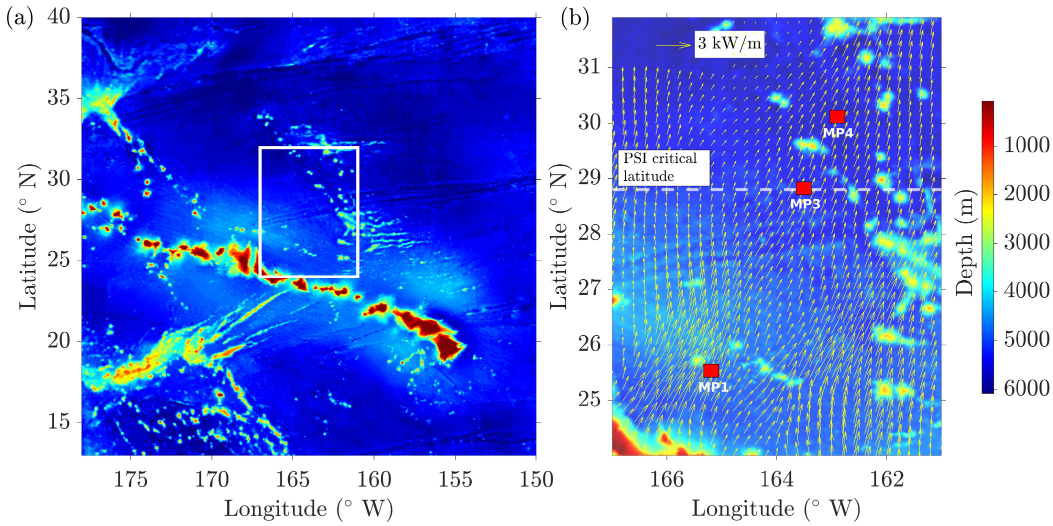

Figure 1. (a) The domain of study north of Hawaii is marked by the white rectangle. (b) An expanded view of the simulation domain. The locations of the McLane moored profilers (MP1, MP3, and MP4) are marked as red solid blocks. Yellow arrows show the energy flux of the mode-1 M_2 internal tide from satellite altimetry (Zhao et al., 2016; Zhao, 2022). The white dashed line at 28.8° N is the critical latitude for parametric subharmonic instability (PSI; e.g., MacKinnon et al., 2013). The model bathymetry from Smith and Sandwell (1997) is shown in color in each subplot.

ulations are identical to those of the LLC4320 simulation upto a certain depth but max out at thicknesses of Δz=100m below 2250m, Δz=50m below 1110m, and Δz=25m below 300m for the 109, 153, and 264-level simulations, respectively (see Fig S1). These regional simulations begin on 1 March 2012 and run for 73 days with initial fields taken from the global LLC4320 simulation, which employs the same grid spacing in the horizontal and 90 z-levels in the vertical direction (Rocha, Chereskin, et al., 2016; Savage et al., 2017). At the lateral boundaries, the regional simulations are forced by fields from the global LLC4320 simulation, which also includes remotely-generated IWs. All the simulations are forced with realistic atmospheric fields and astronomical tidal potential. Velocities, temperature, and salinity are stored at hourly intervals. (More in the SI.)

2.2 Observations

McLane moored profilers (MP) are deployed on oceanographic moorings and vertically profile the water column at 10–33 cm s^{-1} (Doherty et al., 1999). MPs record velocities, temperature, conductivity, pressure, and other oceanic variables in hourly intervals. We use data from three MPs, deployed in the Pacific during the Internal Waves Across the Pacific experiment (Alford et al., 2007) along track 249 of TOPEX-Poseidon. The MP locations are marked as MP1 (194.8° E, 25.5° N), MP3 (196.5° E, 28.8° N), and MP4 (197.1° E, 30.1° N) in Fig 1 (b). The MP data are available in the depth range of 85–1384m with a vertical resolution of ∼2m, from 25 April–05 June 2006 at MP1 and MP3, and from 25 April–17 May 2006 at MP4.

2.3 Spectra calculations

Prior to vertical wavenumber spectra calculations with both model output and MP data, the horizontal velocities and the depths are WKBJ-scaled using local buoyancy frequency following Leaman and Sanford (1975) and interpolated to equally-spaced vertical coordinates (see Fig S2 and text in the SI). All vertical wavenumber spectra presented in this paper are averages of individual spectra over the model runtime and MP deployment periods, giving ∼1700 degrees of freedom (dof) for models and 530–950 dof for MPs assuming the spectra to be mutually independent. Velocities at the top and bottom of the depth range of spectra calculation are smoothly tapered to zero values using a Hanning window, and the lost variance due to this tapering is added back to the total variance. There is no segmenting of data in the vertical direction in our computations of spectra. (More in the SI.)

3 Model parameterizations

The interior vertical mixing parameterization scheme in the simulations is KPP (Large et al., 1994), and the horizontal mixing is governed by the Leith parameterization for 2D turbulence (Leith, 1968). The Leith scheme is modified with an added damping term for the divergent flow field (Fox-Kemper & Menemenlis, 2008). The effect of this modified Leith scheme on the modeled IW fields in high-resolution regional models is not considered here but will be discussed in future studies.

There are three controlling parameters which cumulatively act within the KPP scheme for the ocean interior mixing away from the upper mixed layer: (a) Richardson number-dependent shear-driven mixing, (b) a constant (in both space and time) background mixing to compensate for the breaking of unresolved IWs, set to 5.66×10^{-4} m^{2}s^{-1} as viscosity in the momentum equations and 5.44×10^{-7} m^{2}s^{-1} for temperature and salt diffusivity in LLC4320, and (c) double-diffusive mixing which is not implemented in any of the simulations here. The KPP background has constant damping coefficients for energy dissipation that act at all spatial locations, time steps, and vertical scales of the simulations. Also, if the fluid column becomes convectively unstable, it undergoes immediate mixing in the simulations.

With an increase in vertical resolution, models better capture the small-scale density and velocity fluctuations associated with an improved IW field. This raises the question of whether the KPP background, which parameterizes IW-driven mixing in coarser-resolution models that have reduced IW activity, would still be needed with an increase in model resolution. In the following sections, we quantify the effect of KPP background on the modeled spectra primarily using results from the highest-resolution (264-level) simulations (with results from lower-resolution simulations summarized in the SI).

4 Spectral estimates and discussion

In the high-wavenumber regime, Cairns and Williams (1976)'s revision of the Garrett and Munk (1972, 1975) spectrum—GM76—predicts a universal form of the kinetic energy (KE) spectrum $E(m) \sim m^{-2}$, where m are the (stretched) vertical wavenumbers defined here as the inverse of the stretched depths (also see the SI). The GM76 shear and strain spectra derived from $E(m)$ have spectral slopes of m^0 at high-wavenumbers. However, extensive high-resolution observations have demonstrated that these spectral slopes are variable in different regions of the world's ocean (as reviewed in Polzin and Lvov (2011)). Pollmann (2020) provides a global estimate of these spectral slopes and shows that the slopes deviate significantly from that suggested by the empirical GM76 model. Therefore, in the following discussions, we will consider the observed spectra as the "truth" in our comparison of the modeled and observed spectra and include GM76 spectral slopes as reference.

4.1 Kinetic energy spectra

In our regional domain (Fig 1 (b)), vertical wavenumber spectra of KE from the observations differ from the GM76 slope of m^{-2} (Fig 2). At wavenumbers higher than 0.02 cpm (not shown), observed KE spectral slopes from the MPs are nearer to -2.4. Combined with the frequency spectral slopes at these sites, this value is closer to the induced-diffusion-dominated solutions predicted by wave turbulence theory (e.g., Lvov et al., 2010; Y. Pan et al., 2020) than to the GM76 slope.

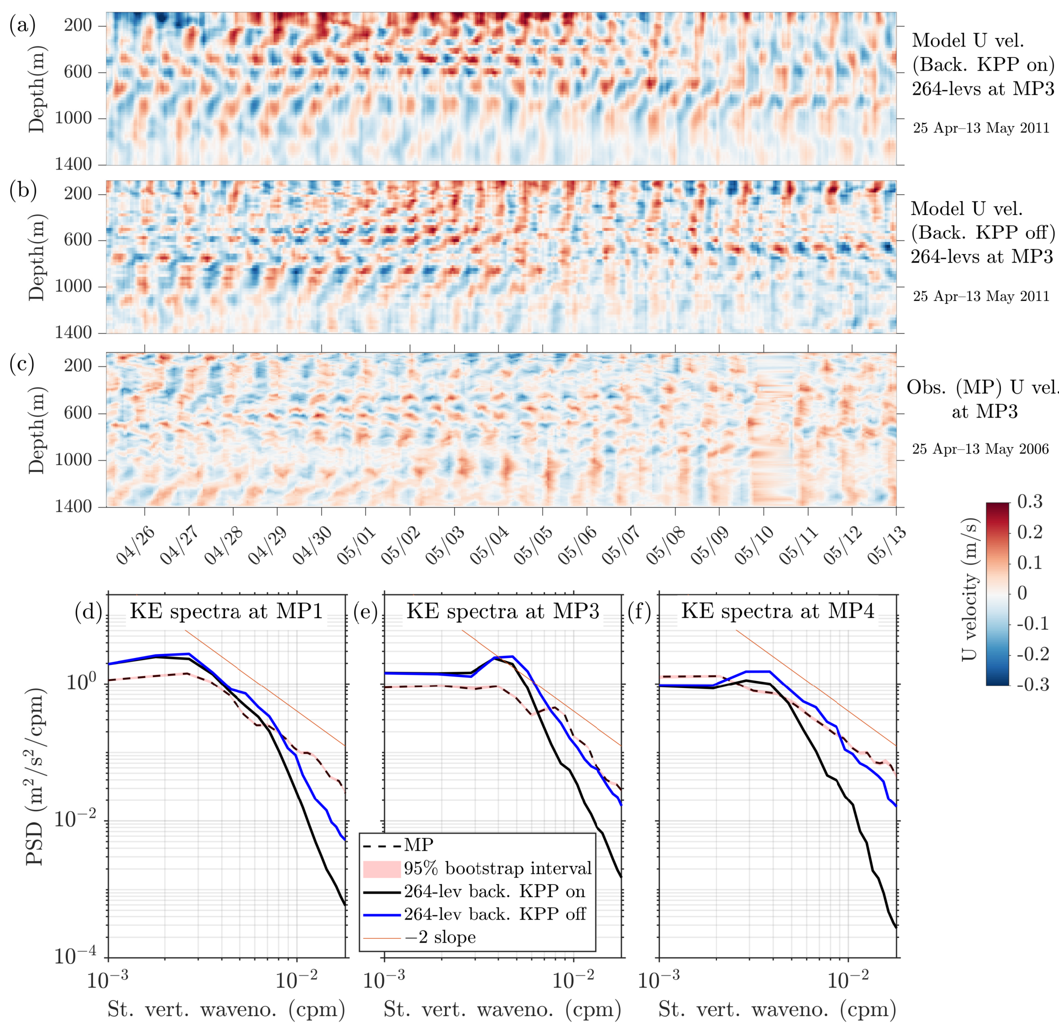

Figure 2. Time-depth plots of zonal (U) velocity from 264-level simulations at the MP3 location and over the depth range of 80–1400 m, with the KPP background (a) on and (b) off, are compared to observed zonal velocity in (c). The model output and the observations are from the same days of the year but different years. In (d–f), KE spectra in the same depth range for 264-level simulations (solid curves) at locations marked in Fig 1 (b) are compared to observed KE spectra (dashed curves) in the depth range of 85–1384m. The solid black curves are the modeled KE spectra with the KPP background on, while the blue curves are the modeled KE spectra with the KPP background components set to zero. 95% bootstrap confidence intervals on the means of the observed KE spectra are drawn in each as light red shading (for simulations, the 95% confidence intervals are smaller than the thickness of the curves). The GM76 spectral slope of −2 is drawn in each for reference. KE spectra are also shown in Figs S3, S4, and S5 in the SI.

We find that the modeled velocities and the KE spectra are sensitive to the KPP background (Fig 2). A comparison of zonal velocities from the 264-level simulations (Fig 2 (a,b)) with that from the observations (Fig 2 (c)) shows that the velocity field has more small-scale features when the KPP background diffusivity and viscosity are both set to zero (Fig 2 (b)). Although a perfect agreement between the velocity field from the simulations and the observations is not expected, energetic events, including those due to tidally-induced periodic flows, have sharper vertical gradients in the simulation without the KPP background (Fig 2 (b)) roughly similar to that seen in the observations (Fig 2 (c)), whereas these gradients are more diffused in the simulation where the KPP background is kept on and has the same values as that of the KPP background in global LLC4320 simulation (Fig 2 (a)).

The effect of turning the KPP background off on the IW field is seen in the comparison of the spectral slopes of the modeled KE spectra to that of the observed KE spectra (Fig 2 (d–f)). At low wavenumbers (<0.003 cpm), both observed and modeled KE spectra with and without KPP background roll off to a limiting slope value near zero. The observed and the modeled spectra disagree within a factor of two at wavenumbers <0.003 cpm at all three MP locations. This disagreement may be due to the differences in the overall oceanic mesoscale variability, tidal or near-inertial fields given that the observations and the model simulations are not contemporaneous. The modeled KE spectra with and without the KPP background diverges at wavenumbers higher than 0.004 cpm in both the cases, suggesting a vertical scale where the KPP background starts to become active in the simulations. This vertical scale has a small variability depending on the geographical location within the domain and the vertical resolution of the model (Fig S3) and is also different in different frequency bands (Fig S4). However, the general conclusion is that the high-wavenumber spectral slopes of the modeled KE spectra with the KPP background turned off lie significantly closer to the observed KE spectra from the MPs (Figs 2 (d–f) and S3).

The greatest improvement in the modeled KE spectra without the KPP background is seen at the MP4 location which is farthest from the generation site of the M_2 tidal beam. The variance at the highest wavenumber is ∼40 times higher at MP4 with the KPP background turned off (Fig 2 (f)). The magnitude of increase in spectral variance at MP1 and MP3 at the highest wavenumber without the KPP background are comparable to each other but less than that at MP4. At MP3, which is ∼500km from the M_2 IT generation site, the improved modeled IW continuum spectral levels are an order of magnitude higher when the KPP background is turned off (Fig 2 (e)), and the levels display a good agreement with the observed KE spectrum. However, the improved modeled spectrum at MP1 is still relatively deficient in the IW continuum. As all the locations have similar vertical stratification, this difference in the spectral improvement and the disagreement between the modeled and the observed spectra could most likely be due to the degree of proximity to the IT generation site. With MP1 being nearer to the IT generation site (Fig 1 (b)), the nonlinear interactions giving rise to the IW continuum have insufficient time to develop, when compared to MP3 or MP4, giving rise to a weaker overall KE spectrum.

Spectral improvement with the KPP background turned off is also observed in the 109- and 153-level simulations (Fig S3) signifying that in both high (264-level) and moderate vertical resolution simulations (109- and 153-levels), the KPP background may have to be turned off to achieve a realistic IW continuum in regional models. We also note that turning off the KPP background improves the modeled IW continuum at all frequencies as the high-wavenumber spectral variances are higher in both the highpass (high-frequency or supertidal) and lowpass frequency bands around a cutoff of 11.5 hr as well as in the semidiurnal and near-inertial frequency bands (shown for 264-level in Fig S4). The lowpass band includes semidiurnal and diurnal tides, and near-inertial and subtidal flows, while the highpass band includes the supertidal IW continuum. We further observe that the high-wavenumber KE variance in the deeper ocean (1500–4000m) progressively increases with an increase in the model vertical resolution (Fig S5).

4.2 Shear and strain spectra

The vertical shear spectrum is defined as $\Phi(m) = (2\pi m)^2 E(m)$ (Gregg et al., 1993). In what follows, we first describe the shear characteristics of the regional domain using MP observations and then compare it to the shear spectra from the 264-level simulation with the KPP background turned off to understand the strengths and deficiencies of the modeled shear in different frequency bands.

The observed shear from MPs is dominated by slowly-varying (lowpass) flows with periods greater than 11.5 hr at all vertical scales (Fig 3 (a, c, e)). As expected, the NI band contributes significantly to the total shear. Alford et al. (2017) find that the shear layers at the PSI latitude (MP3) persist for $\mathcal{O}(25)$ days. In contrast, the shear layers persist for $\mathcal{O}(7)$ days at other MP locations. This is reflected in the NI shear spectrum at MP3 which has the highest variance among the three locations (Fig 3 (c) compared to (a, e)). The NI

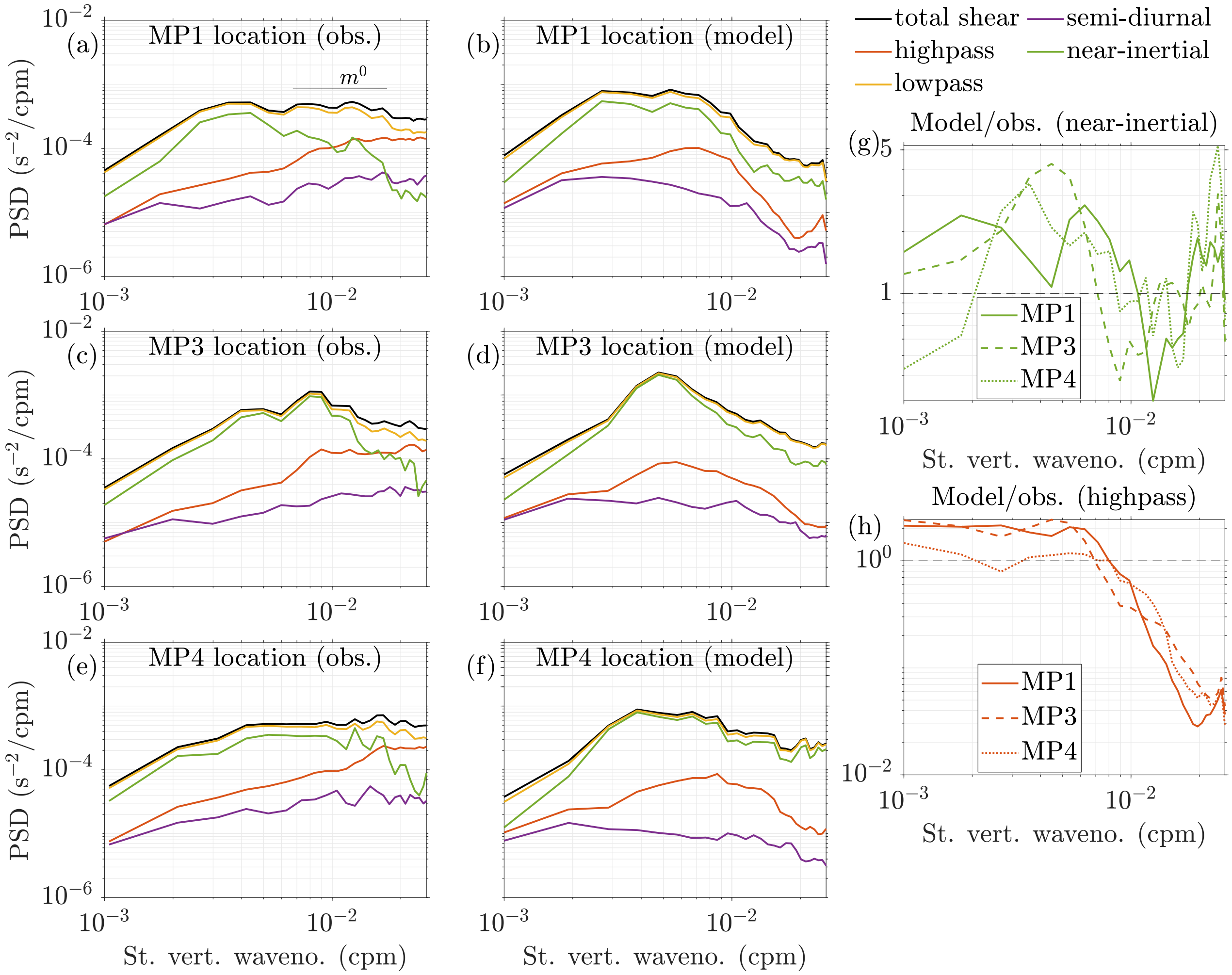

Figure 3. Shear spectra $\Phi(m)$ in different frequency bands from MP observations in (a), (c), and (e) are compared to modeled shear spectra from the 264-level simulation with the KPP background turned off in (b), (d), and (f). In each subplot, black is total shear, red is highpass or supertidal shear (>11.5 hr), yellow is lowpass shear (<11.5 hr), purple is semi-diurnal shear (11.5–13.5 hr), and green is NI shear (90–110% of the local inertial period). The high-wavenumber m^0 slope of the GM76 shear spectrum is denoted in (a). (g–h) The ratio of the modeled shear to observed shear, for the NI and highpass bands, respectively.

shear spectra have positive slopes up to 0.003 cpm at MP1 and ∼0.01 cpm at MP3 and MP4, after which they lose variances by an order of magnitude at MP1 and MP3. However, the NI shear at MP4 does not have much vertical variability and also has lower peak shear variance. The NI shear is geographically variable at small vertical scales in that it is a factor of 2–5 lower than the total shear at the highest wavenumber at MP3 and MP4 but approximately 20 times lower at MP1. The highpass shear is lower than the NI shear at low wavenumbers but has a higher variance than the NI shear above 0.01 cpm.

Similar to the observations, the modeled 264-level shear with the KPP background turned off is dominated by slowly-varying flows (Fig 3 (b, d, f)). The integrated modeled shear at the PSI latitude (MP3; Fig 3 (d)) is 1.2–2.5 times higher than at MP1 and MP4 (Fig 3 (b, f)) and attains the highest peak shear among the three locations. Considering the ratio of variance in the NI band (Fig 3 (g)), the modeled and the observed shear show reasonable agreement. In the highpass band, the model does not capture the transition as seen in the observed shear at 0.01 cpm as the modeled highpass shear remains lower than the respective modeled NI shear at all wavenumbers (e.g., comparing Fig 3 (a) and (b)). The ratio of the modeled to observed highpass shear (Fig 3 (h)) shows that in contrast to the other two locations, the modeled highpass shear at MP4 is within a factor of 1.5 of the observed highpass shear for a decade of wavenumbers from 10^{-3}–10^{-2} cpm. However, unlike the NI shear ratio, the modeled to observed highpass shear ratio decreases after 0.007–0.008 cpm and the modeled highpass shear is more than an order of magnitude less than the observations at the highest wavenumber (Fig 3 (h)). This reduction in high-wavenumber highpass shear variance could be attributed to the inability of the model to represent the cascade of energy to these vertical scales from low-frequency and NI motions due to a model grid spacing that is too coarse (see section 4 in the SI) or excessive damping by improper model parameterizations.

The modeled spectra of strain $(\mathrm{N}^2 - \overline{\mathrm{N}^2})/\overline{\mathrm{N}^2}$, with N being the Brunt–Väisälä frequency and overbar denoting time mean, are lower in variance relative to the observed strain spectra (Fig 4 (a–c)). Except in the small range of 0.003–0.004 cpm at the MP1 location (Fig 4 (a)), the model is always lower than the observations in strain variance even in the highest resolution (264-level) simulations. Turning off the KPP background increases the strain variance by less than an order of magnitude at high wavenumbers, but this increase is not sufficient enough to bring the modeled strain variance up to the level of the observations. The largest increase in variance by turning off the KPP background is seen at MP4 (Fig 4 (c)), the location farthest from the IT generation site (Fig 1 (b)). Except in the NI band and over a small range of wavenumbers, the modeled strain variance is an order of magnitude too low over the majority of the wavenumbers in all frequency bands (Fig S6). In the deeper ocean (below 1500m), an appreciable increase in the representation of modeled small-scale strain is observed when the vertical resolution of the model is progressively increased (shown for a small depth range of 1800–2200m in Fig 4 (d–f)). This improvement with an increase in the model vertical resolution is reflected in the deep-ocean (1500–4000m) strain spectra (Fig S7) which have the highest variance in the 264-level simulations. Improving the modeled strain may involve refined temporal and spatial resolution as well as understanding the effect of other model parameterizations.

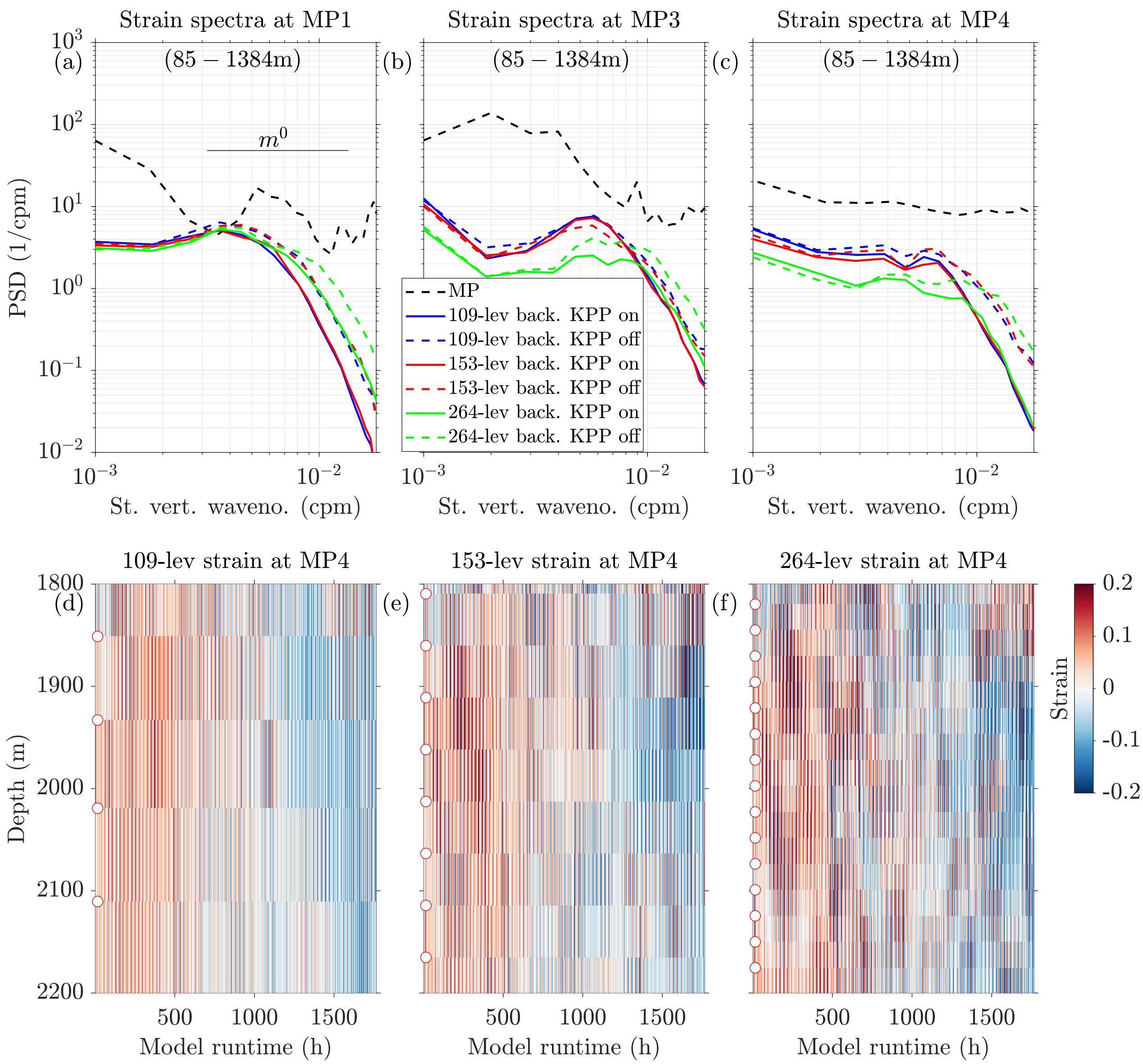

Figure 4. (a–c) Observed strain spectra (black dashed curves) for different locations in the depth range of 85–1384m are compared to modeled strain spectra from 109-, 153-, and 264-level simulations in the depth range of 80–1400m with and without the KPP background components. (d–f) Time-depth plots of the deeper ocean (1800–2200m) modeled strain at MP4 location without the KPP background components for three different vertical resolutions of the model. The filled circles on the y-axis are the locations of the model z-levels. The ratios of the modeled to observed strain in different frequency bands are in Fig S6 and the modeled strain spectra in the deep ocean (1500–4000m) are in Fig S7.

5 Conclusions

Regional simulations with higher vertical and horizontal resolutions can display improved IW spectra over those in the global simulations, as long as they are forced at their lateral boundaries by remotely-generated IWs from global simulations (Mazloff et al., 2020; Nelson et al., 2020). High vertical resolution regional simulations at the same horizontal grid spacing ($\sim$2km) as the global LLC4320 are studied in this paper to explore the sensitivities of the modeled IW vertical structure to model parameterizations, in particular, the background mixing components of the K-Profile Parameterization (KPP; Large et al. (1994)). We show that the kinetic energy variance at the high vertical-wavenumber IW continuum increases and lies closer to the observations when the KPP background components are set to zero, with the agreement most notable in locations away from the tidal generation site of the Hawaiian islands. Thus, when high-resolution ocean models start resolving IWs, the KPP background, which compensates for breaking IWs in coarse-grid models that do not represent IW processes at all, should be turned down or even off to maintain the proper spectral level of the IW continuum.

The higher shear at the parametric subharmonic instability critical latitude is captured in the simulations with the KPP background turned off. The ability of the model to represent near-inertial shear, a critical component of the total IW shear, at all vertical wavenumbers is an encouraging start in understanding the space-time variability of IW shear using ocean models. However, the high-frequency or supertidal (>11.5 hr) component of the IW continuum shear is not adequately captured in this model. The simulations with the KPP background turned off are weaker in strain variance relative to the observed strain. The increase in modeled strain variance with the KPP background turned off is not enough to elevate the modeled spectral levels to that of the observations. This work can be developed in a few directions to address these model deficiencies and further improve the modeled IW continuum. We have not studied the sensitivity of the modeled spectra to the frequency of atmospheric forcing updates. We have also not explored the effects of increasing the horizontal resolution and the role of other model mixing parameterizations, most importantly, the Leith damping and the Richardson number-dependent shear-driven mixing component of the KPP and to what extent these govern mixing without the background components. These issues are likely to be important for accurate modeling of high-frequency shear and strain and will be discussed in future papers.

Acknowledgments

RT and BKA were supported by NASA grant 80NSSC20K1135 and NSF grant OCE-1851164. WRP was supported by the Natural Sciences and Engineering Research Council of Canada under the NSERC Discovery grant A9627. DM carried out research at JPL, Caltech, under contract with NASA, with support from the Physical Oceanography and Modeling, Analysis, and Prediction Programs. All the simulations in this study were performed on the Niagara supercomputer of the SciNet facility of the University of Toronto, which is a component of the Compute Canada HPC platform. The MP observations from Alford et al. (2007) were funded by NSF, and would not have been possible without the hard work and talent of the captain and crews of several ships and the Wavechasers engineering group at the Applied Physics Laboratory / UW. Energy flux of the mode-1 M_2 internal tide was provided by Zhongxiang Zhao. Reviews by Clément Vic and one other anonymous reviewer greatly helped improve this paper including the addition of the supplementary Fig S8 and more about model resolution. RT thanks Arin D. Nelson for initial discussions.

6 Open Research

The McLane moored profiler observations, regional MITgcm model simulation output, and the analysis codes used in this study are hosted at Harvard Dataverse at `https://doi.org/10.7910/DVN/HOVAPO`. The global LLC4320 simulation output is available at `https://data.nas.nasa.gov/ecco/`.

References

Adcroft, A., Campin, J.-M., Doddridge, S. D., Evangelinos, C., Ferreira, D., Follows, M., ... others (2018). Mitgcm documentation. *Release checkpoint67a-12-gbf23121*, *19*. Retrieved from `https://buildmedia.readthedocs.org/media/pdf/mitgcm/latest/mitgcm.pdf` (Accessed: 12-29-2021)

Alford, M. H., MacKinnon, J., Zhao, Z., Pinkel, R., Klymak, J., & Peacock, T. (2007). Internal waves across the Pacific. *Geophysical Research Letters*, *34*(24).

Alford, M. H., MacKinnon, J. A., Pinkel, R., & Klymak, J. M. (2017). Space–time scales of shear in the North Pacific. *Journal of Physical Oceanography*, *47*(10), 2455–2478.

Alford, M. H., MacKinnon, J. A., Simmons, H. L., & Nash, J. D. (2016). Near-inertial internal gravity waves in the ocean. *Annual Review of Marine Science*, *8*, 95–123.

Alford, M. H., Simmons, H. L., Marques, O. B., & Girton, J. B. (2019). Internal tide attenuation in the North Pacific. *Geophysical Research Letters*, *46*(14), 8205–8213.

Arbic, B. K., Alford, M. H., Ansong, J. K., Buijsman, M. C., Ciotti, R. B., Farrar, J. T., ... others (2018). A primer on global internal tide and internal gravity wave continuum modeling in HYCOM and MITgcm. In E. Chassignet, A. Pascual, J. Tintoré, & J. Verron (Eds.), *New Frontiers in Operational Oceanography* (pp. 307–392). GODAE OceanView.

Baines, P. G. (1982). On internal tide generation models. *Deep Sea Research Part A. Oceanographic Research Papers*, *29*(3), 307–338.

Barkan, R., Winters, K. B., & McWilliams, J. C. (2017). Stimulated imbalance and the enhancement of eddy kinetic energy dissipation by internal waves. *Journal of Physical Oceanography*, *47*(1), 181–198.

Bell, T. (1975). Topographically generated internal waves in the open ocean. *Journal of Geophysical Research*, *80*(3), 320–327.

Cairns, J. L., & Williams, G. O. (1976). Internal wave observations from a midwater float, 2. *Journal of Geophysical Research*, *81*(12), 1943–1950.

D'Asaro, E. A., & Morison, J. H. (1992). Internal waves and mixing in the Arctic Ocean. *Deep Sea Research Part A. Oceanographic Research Papers*, *39*(2), S459–S484.

Doherty, K., Frye, D., Liberatore, S., & Toole, J. (1999). A moored profiling instrument. *Journal of Atmospheric and Oceanic Technology*, *16*(11), 1816–1829.

Fox-Kemper, B., & Menemenlis, D. (2008). Can large eddy simulation techniques improve mesoscale rich ocean models? *Washington DC American Geophysical Union Geophysical Monograph Series*, *177*, 319–337.

Garrett, C., & Munk, W. (1972). Space-time scales of internal waves. *Geophysical Fluid Dynamics*, *3*(3), 225–264.

Garrett, C., & Munk, W. (1975). Space-time scales of internal waves: A progress report. *Journal of Geophysical Research*, *80*(3), 291–297.

Gregg, M., Winkel, D., & Sanford, T. (1993). Varieties of fully resolved spectra of vertical shear. *Journal of Physical Oceanography*, *23*(1), 124–141.

Kunze, E. (2017a). The internal-wave-driven meridional overturning circulation. *Journal of Physical Oceanography*, *47*(11), 2673–2689.

Kunze, E. (2017b). Internal-wave-driven mixing: Global geography and budgets. *Journal of Physical Oceanography*, *47*(6), 1325–1345.

Large, W. G., McWilliams, J. C., & Doney, S. C. (1994). Oceanic vertical mixing: A review and a model with a nonlocal boundary layer parameterization. *Reviews of Geophysics*, *32*(4), 363–403.

Large, W. G., & Yeager, S. G. (2004). *Diurnal to decadal global forcing for ocean and sea-ice models: The data sets and flux climatologies* (Tech. Rep.). University Corporation for Atmospheric Research. Retrieved from http://dx.doi.org/10.5065/D6KK98Q6

Leaman, K. D., & Sanford, T. B. (1975). Vertical energy propagation of inertial waves: A vector spectral analysis of velocity profiles. *Journal of Geophysical Research*, *80*(15), 1975–1978.

Leith, C. E. (1968). Diffusion approximation for two-dimensional turbulence. *The Physics of Fluids*, *11*(3), 671–672.

Losch, M., Menemenlis, D., Campin, J.-M., Heimbach, P., & Hill, C. (2010). On the formulation of sea-ice models. Part 1: Effects of different solver implementations and parameterizations. *Ocean Modelling*, *33*(1-2), 129–144.

Lvov, Y. V., Polzin, K. L., Tabak, E. G., & Yokoyama, N. (2010). Oceanic internal-wave field: Theory of scale-invariant spectra. *Journal of Physical Oceanography*, *40*(12), 2605–2623.

MacKinnon, J. A., Alford, M. H., Sun, O., Pinkel, R., Zhao, Z., & Klymak, J. (2013). Parametric subharmonic instability of the internal tide at 29 N. *Journal of Physical Oceanography*, *43*(1), 17–28.

MacKinnon, J. A., Zhao, Z., Whalen, C. B., Waterhouse, A. F., Trossman, D. S., Sun, O. M., ... others (2017). Climate process team on internal wave–driven ocean mixing. *Bulletin of the American Meteorological Society*, *98*(11), 2429–2454.

Marshall, J., Adcroft, A., Hill, C., Perelman, L., & Heisey, C. (1997). A finite-volume, incompressible Navier Stokes model for studies of the ocean on parallel computers. *Journal of Geophysical Research: Oceans*, *102*(C3), 5753–5766.

Mazloff, M. R., Cornuelle, B., Gille, S. T., & Wang, J. (2020). The importance of remote forcing for regional modeling of internal waves. *Journal of Geophysical Research: Oceans*, *125*(2), e2019JC015623.

Menemenlis, D., Campin, J.-M., Heimbach, P., Hill, C., Lee, T., Nguyen, A., ... Zhang, H. (2008). ECCO2: High resolution global ocean and sea ice data synthesis. *Mercator Ocean Quarterly Newsletter*, *31*(October), 13–21.

Morrison, A., Toole, J., Lukas, R., Worrilow, S., & Doherty, K. (2001). Results from the first successful field deployment of the McLane moored profiler. In *MTS/IEEE Oceans*

2001. An Ocean Odyssey. Conference Proceedings (IEEE Cat. No.01CH37295) (Vol. 2, p. 949-955).

Müller, M., Arbic, B. K., Richman, J. G., Shriver, J. F., Kunze, E. L., Scott, R. B., ... Zamudio, L. (2015). Toward an internal gravity wave spectrum in global ocean models. *Geophysical Research Letters*, *42*(9), 3474–3481.

Munk, W., & Wunsch, C. (1998). Abyssal recipes II: Energetics of tidal and wind mixing. *Deep Sea Research Part I: Oceanographic Research Papers*, *45*(12), 1977–2010.

Nelson, A., Arbic, B., Menemenlis, D., Peltier, W., Alford, M., Grisouard, N., & Klymak, J. (2020). Improved internal wave spectral continuum in a regional ocean model. *Journal of Geophysical Research: Oceans*, *125*(5), e2019JC015974.

Pan, X., Wong, G. T., Shiah, F.-K., & Ho, T.-Y. (2012). Enhancement of biological productivity by internal waves: observations in the summertime in the northern South China Sea. *Journal of Oceanography*, *68*(3), 427–437.

Pan, Y., Arbic, B. K., Nelson, A. D., Menemenlis, D., Peltier, W., Xu, W., & Li, Y. (2020). Numerical investigation of mechanisms underlying oceanic internal gravity wave power-law spectra. *Journal of Physical Oceanography*, *50*(9), 2713–2733.

Pollmann, F. (2020). Global characterization of the oceans internal wave spectrum. *Journal of Physical Oceanography*, *50*(7), 1871–1891.

Polzin, K. L., & Lvov, Y. V. (2011). Toward regional characterizations of the oceanic internal wavefield. *Reviews of Geophysics*, *49*(4).

Rocha, C. B., Chereskin, T. K., Gille, S. T., & Menemenlis, D. (2016). Mesoscale to submesoscale wavenumber spectra in Drake Passage. *Journal of Physical Oceanography*, *46*(2), 601–620.

Rocha, C. B., Gille, S. T., Chereskin, T. K., & Menemenlis, D. (2016). Seasonality of submesoscale dynamics in the Kuroshio Extension. *Geophysical Research Letters*, *43*(21), 11,30411,311.

Savage, A. C., Arbic, B. K., Alford, M. H., Ansong, J. K., Farrar, J. T., Menemenlis, D., ... others (2017). Spectral decomposition of internal gravity wave sea surface height in global models. *Journal of Geophysical Research: Oceans*, *122*(10), 7803–7821.

Smith, W. H., & Sandwell, D. T. (1997). Global sea floor topography from satellite altimetry and ship depth soundings. *Science*, *277*(5334), 1956–1962.

Su, Z., Wang, J., Klein, P., Thompson, A. F., & Menemenlis, D. (2018). Ocean submesoscales as a key component of the global heat budget. *Nature Communications*, *9*(1), 1–8.

van Haren, H. (2016). Do deep-ocean kinetic energy spectra represent deterministic or stochastic signals? *Journal of Geophysical Research: Oceans*, *121*(1), 240–251.

Welch, P. (1967). The use of fast Fourier transform for the estimation of power spectra: a method based on time averaging over short, modified periodograms. *IEEE Transactions on Audio and Electroacoustics*, *15*(2), 70–73.

Whalen, C. B., de Lavergne, C., Garabato, A. C. N., Klymak, J. M., Mackinnon, J. A., & Sheen, K. L. (2020). Internal wave-driven mixing: governing processes and consequences for climate. *Nature Reviews Earth & Environment*, *1*(11), 606–621.

Wunsch, C., & Ferrari, R. (2004). Vertical mixing, energy, and the general circulation of the oceans. *Annual Review of Fluid Mechanics*, *36*(1), 281–314.

Zhao, Z. (2022). Development of the yearly mode-1 M_2 internal tide model in 2019. *Journal of Atmospheric and Oceanic Technology*, *39*(4), 463–478.

Zhao, Z., Alford, M. H., Girton, J. B., Rainville, L., & Simmons, H. L. (2016). Global observations of open-ocean mode-1 M_2 internal tides. *Journal of Physical Oceanography*, *46*(6), 1657–1684.

Zhao, Z., Alford, M. H., MacKinnon, J. A., & Pinkel, R. (2010). Long-range propagation of the semidiurnal internal tide from the Hawaiian Ridge. *Journal of Physical Oceanography*, *40*(4), 713–736.

Supporting Information for "Impact of vertical mixing parameterizations on internal gravity wave spectra in regional ocean models"

Ritabrata Thakur[1], Brian K. Arbic[1], Dimitris Menemenlis[2], Kayhan Momeni[3], Yulin Pan[4], W. R. Peltier[3], Joseph Skitka[1], Matthew H. Alford[5], Yuchen Ma[3]

[1]Department of Earth and Environmental Sciences, University of Michigan, Ann Arbor, MI, USA

[2]Jet Propulsion Laboratory, California Institute of Technology, Pasadena, CA, USA

[3]Department of Physics, University of Toronto, Toronto, Canada

[4]Department of Naval Architecture and Marine Engineering, University of Michigan, Ann Arbor, MI, USA

[5]Scripps Institution of Oceanography, University of California San Diego, La Jolla, CA, USA

In this supporting information (SI) section, we first describe the details of the ocean simulations in section 1. We then describe the methodology of calculating "WKBJ-stretched" depths in section 2 and the methodology of computing vertical wave-number spectra in section 3. We discuss the model resolution and the resolved internal wave field in section 4.

Corresponding author: Ritabrata Thakur. Suite 2534, Department of Earth and Environmental Sciences, University of Michigan, Ann Arbor, MI 48109, USA. (ritabrata90official@gmail.com)

The vertical level thicknesses of the simulations are shown in Fig S1 and the relationship between actual ocean depth and the WKBJ-stretched depth is in Fig S2. We show the sensitivity of the kinetic energy (KE) spectra at three different vertical resolutions of the model to the background mixing components of the K-Profile Parameterization (KPP) by comparing them with the KE spectra from McLane moored profilers (MP) in Fig S3. The effect of KPP background components in different frequency bands of the modeled KE spectra for the 264-level simulation is seen in Fig S4 where we see that in all the frequency bands, the modeled KE spectra with the KPP background turned off have a higher variance in the IW continuum. We find that the deep ocean (1500–4000 m) modeled KE spectra are sensitive to model vertical resolution as they progressively include more variance in the IW continuum with an increase in model vertical resolution (Fig S5). In S6, the ratios of modeled strain to MP strain in different frequency bands show that the model always has lower high-wavenumber strain. In Fig S7, we show the deep ocean (1500–4000 m) modeled strain spectra and see improvement in strain variance with an increase in model resolution. In Fig S8, we discuss the resolved internal wave scales in the 264-level simulation when compared to the full ocean internal wave field.

1. Global and regional simulations

The numerical simulations in this study were carried out using a hydrostatic configuration of the Massachusetts Institute of Technology general circulation model (MITgcm; Marshall, Adcroft, Hill, Perelman, and Heisey (1997); Adcroft et al. (2018)). The global simulation which forces the regional simulations in this paper has previously been referred to as LLC4320 (Rocha et al., 2016) and MITgcm48 (Savage et al., 2017). This global simulation has a horizontal grid spacing of 1/48° (∼2 km in the simulation domain) and 90 vertical levels with a surface level thickness of 1m which progressively increases with depth to a maximum thickness of 480m (Fig S1). The model depth is approximately 6 km in the deepest parts of the domain. The LLC4320 simulation uses a Latitude-Longitude-polar Cap (LLC) horizontal grid configuration and includes a dynamic/thermodynamic sea ice model (Losch et al., 2010). A progressive spin-up strategy was employed, starting from a data-constrained, 1/6° simulation (Menemenlis et al., 2008) and progressing through a 1-year simulation at 1/12° and an 8-month simulation at 1/24°. The integration time step for the LLC4320 simulation is 25 s. For our purposes, we use hourly snapshots of the model output. The model setup of the global LLC4320 simulation can be found at `http://mitgcm.org/viewvc/MITgcm/MITgcm_contrib/llc_hires` and the model output at `https://data.nas.nasa.gov/ecco/`.

The regional simulations in this paper have three different vertical grid spacings (see Fig S1), while the horizontal grid spacing is identical to that of the global LLC4320 simulation. The regional simulations begin on 1 March 2012 with the initial state from LLC4320 interpolated onto the requisite vertical grid. These simulations are forced by realistic atmospheric and astronomical tidal forcing (Arbic et al., 2018). The wind and other surface variables like temperature and humidity are updated on a 6-hourly basis from 0.14° European Center for Medium-Range Weather Forecasts (ECMWF) analysis starting in 2011. The atmospheric fields are converted to surface fluxes using the bulk formulae of Large and Yeager (2004). At every model time step, a hard boundary condition without the use of a sponge layer is enforced at the lateral boundaries of the regional model to match the fields of the regional simulation to that of the global LLC4320 simulation. The horizontal mixing is prescribed based on the modified Leith scheme of Fox-Kemper and Menemenlis (2008) and the vertical mixing by the K-Profile Parameterization (KPP) of Large, McWilliams, and Doney (1994). The model uses the ocean bathymetry of Smith and Sandwell (1997). With a change in the vertical level thicknesses of the regional simulations, the integration time step also need to be adjusted. The highest vertical resolution (264-level) simulation has a time step of 10 s, the 153-level simulation uses 15 s, and the lowest vertical resolution (109-level) simulation was run with a time step of 25 s, the latter being the same as the global LLC4320 time step. We use hourly snapshots of model output from these regional simulations in all of our analyses. The regional simulation output and the analysis codes can be found at `https://doi.org/10.7910/DVN/HOVAPO`.

2. WKBJ-stretched depths

Internal wave propagation is affected by changes in ocean stratification. To account for the effect of variable stratification in computing the vertical wavenumber spectra, both velocity and depths from model and MP observations need to be normalised by the buoyancy frequency. The horizontal velocities are scaled by $(\overline{\mathrm{N}}(z)/\mathrm{N}_0)^{1/2}$, where $\mathrm{N}(z)$ is the Brunt–Väisälä frequency with the overbar denoting time average for the model run time or the MP deployment time, and the constant $\mathrm{N}_0 = 3$ cph following Leaman and Sanford (1975). The "WKBJ-stretched" or buoyancy-frequency-stretched depths (z_s) are estimated according to the differential equation $dz_s = (\overline{\mathrm{N}}(z)/\mathrm{N}_0)\mathrm{d}z$. The vertical wavenumbers are then $1/\Delta z_s$ in units of cycles per stretched-meter (cpm). An example relationship between the actual ocean depths and the stretched depths for the 264-level model is shown in Fig S2 (a) and the buoyancy frequency profile used for scaling is shown in Fig S2 (b). The vertical wavenumber spectra presented in this paper are based on the stretched depths.

3. Spectral estimates

The vertical wavenumber spectra are calculated as time averages of individual one-dimensional spectra of the fields in the vertical direction. For the simulations, the spectra are averaged over approximately 73 days of model runs and for the deployment days of the MPs. The means and linear trends are removed from the model output and MP data before spectra calculations. A Hanning window is used to taper the velocities, temperature, and salinity at the vertical ends of the water column for all the spectral calculations. The reduced variances due to this tapering are added back into the spectral estimates. Ocean vertical velocities are generally smaller than horizontal velocities and hence not included here due to greater uncertainties in their measurements. Due to the relatively low number of grid points in the vertical direction (40 points for the 109-level and 58 points for the 264-level model in the 80–1400 m depth range), we use the whole water column to calculate the spectra for both model and MP, i.e., there is no segmenting of the velocities and scalar field involved unlike that used in traditional frequency spectra calculation using overlapping segments (e.g., the Welch periodogram method (Welch, 1967)). The highpass and the lowpass definition used in this paper have a cutoff of 11.5 hr and are hence the supertidal and subtidal frequency bands. The near-inertial band is

90–110% of the local inertial period at each MP location. The inertial period is 27.84 hr at MP1 and 23.92 hr at MP4.

4. A note on resolved internal wave field

The approximate wavenumber bounds of the ocean internal wave field are shown in Fig S8. Lines of constant internal wave frequencies ω are drawn using the dispersion relation $\omega^2 = (f^2m^2 + \mathrm{N}^2k^2)/(k^2 + m^2)$, where f is the inertial period at 30° N, $\mathrm{N} = \mathrm{N}_0 = 3$ cph, k are the horizontal wavenumbers, and m are the stretched vertical wavenumbers. The red rectangle in Fig S8 shows the scales resolved by the 264-level simulations.

The modeled highpass shear is low in variance for vertical wavenumbers greater than 0.007–0.008 cpm (Fig 3 (h)) and is more than an order of magnitude lower than the observations at the highest resolvable wavenumber. Fig S8 shows that for vertical wavenumbers higher than, say, 0.007–0.008 cpm, the model captures only a small portion of the highpass band (the area between the orange line and the red rectangle above vertical wavenumber 0.007 cpm). This limitation in model horizontal resolution could be responsible for the reduced variance in the modeled highpass shear and probably also for high wavenumber strain. Future simulations will include finer horizontal resolution aimed towards resolving the smallest internal wave scales, although this will be extremely expensive in terms of computational cost and data storage.

References

Adcroft, A., Campin, J.-M., Doddridge, S. D., Evangelinos, C., Ferreira, D., Follows, M., ... others (2018). Mitgcm documentation. *Release checkpoint67a-12-gbf23121*, *19*. Retrieved from `https://buildmedia.readthedocs.org/media/pdf/mitgcm/`

latest/mitgcm.pdf (Accessed: 12-29-2021)

Arbic, B. K., Alford, M. H., Ansong, J. K., Buijsman, M. C., Ciotti, R. B., Farrar, J. T., ... others (2018). A primer on global internal tide and internal gravity wave continuum modeling in HYCOM and MITgcm. In E. Chassignet, A. Pascual, J. Tintoré, & J. Verron (Eds.), *New Frontiers in Operational Oceanography* (pp. 307–392). GODAE OceanView.

Fox-Kemper, B., & Menemenlis, D. (2008). Can large eddy simulation techniques improve mesoscale rich ocean models? *Washington DC American Geophysical Union Geophysical Monograph Series*, *177*, 319–337.

Large, W. G., McWilliams, J. C., & Doney, S. C. (1994). Oceanic vertical mixing: A review and a model with a nonlocal boundary layer parameterization. *Reviews of Geophysics*, *32*(4), 363–403.

Large, W. G., & Yeager, S. G. (2004). *Diurnal to decadal global forcing for ocean and sea-ice models: The data sets and flux climatologies* (Tech. Rep.). University Corporation for Atmospheric Research. Retrieved from http://dx.doi.org/10.5065/D6KK98Q6

Leaman, K. D., & Sanford, T. B. (1975). Vertical energy propagation of inertial waves: A vector spectral analysis of velocity profiles. *Journal of Geophysical Research*, *80*(15), 1975–1978.

Losch, M., Menemenlis, D., Campin, J.-M., Heimbach, P., & Hill, C. (2010). On the formulation of sea-ice models. Part 1: Effects of different solver implementations and parameterizations. *Ocean Modelling*, *33*(1-2), 129–144.

Marshall, J., Adcroft, A., Hill, C., Perelman, L., & Heisey, C. (1997). A finite-volume, incompressible Navier Stokes model for studies of the ocean on parallel computers. *Journal of Geophysical Research: Oceans*, *102*(C3), 5753–5766.

Menemenlis, D., Campin, J.-M., Heimbach, P., Hill, C., Lee, T., Nguyen, A., ... Zhang, H. (2008). ECCO2: High resolution global ocean and sea ice data synthesis. *Mercator Ocean Quarterly Newsletter*, *31*(October), 13–21.

Rocha, C. B., Chereskin, T. K., Gille, S. T., & Menemenlis, D. (2016). Mesoscale to submesoscale wavenumber spectra in Drake Passage. *Journal of Physical Oceanography*, *46*(2), 601–620.

Savage, A. C., Arbic, B. K., Alford, M. H., Ansong, J. K., Farrar, J. T., Menemenlis, D., ... others (2017). Spectral decomposition of internal gravity wave sea surface height in global models. *Journal of Geophysical Research: Oceans*, *122*(10), 7803–7821.

Smith, W. H., & Sandwell, D. T. (1997). Global sea floor topography from satellite altimetry and ship depth soundings. *Science*, *277*(5334), 1956–1962.

Welch, P. (1967). The use of fast Fourier transform for the estimation of power spectra: a method based on time averaging over short, modified periodograms. *IEEE Transactions on Audio and Electroacoustics*, *15*(2), 70–73.

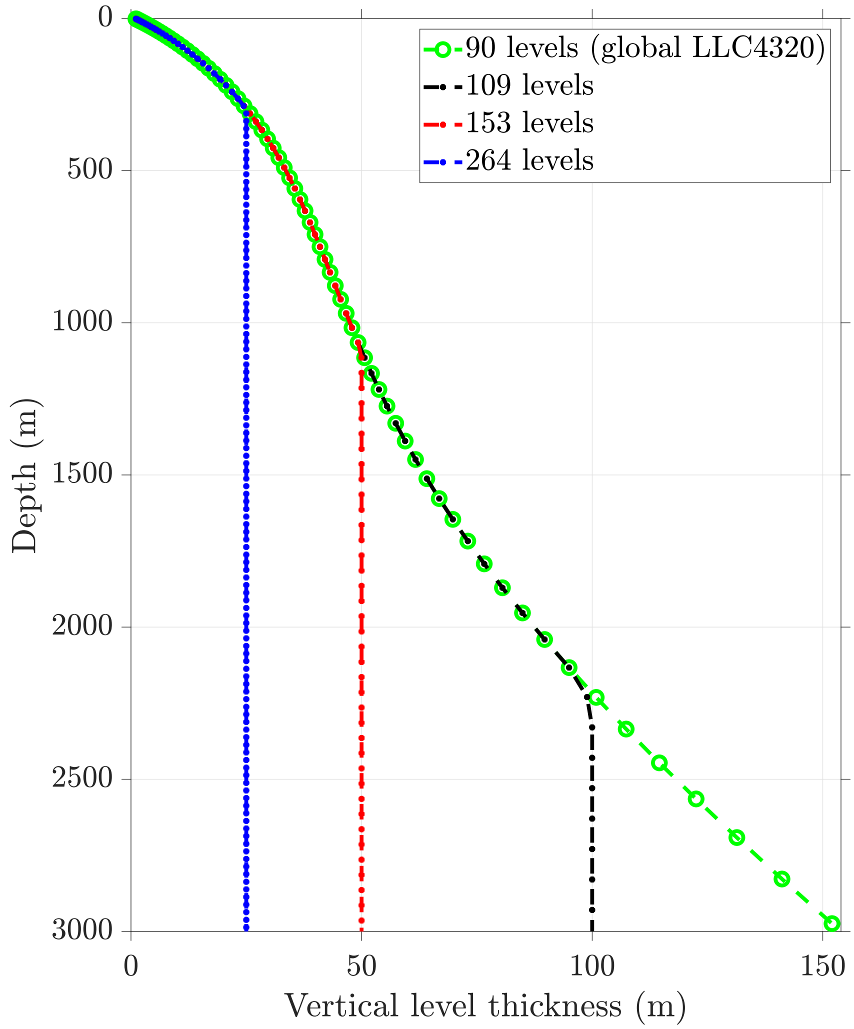

Figure S1. Model vertical level thickness is plotted against ocean depth for the 109-level (black curve with dots), 153-level (red curve with dots), and 264-level (blue curve with dots) regional MITgcm simulations. The vertical level thickness of the global LLC4320 simulation are shown with the green curve with circles. All have the same horizontal grid spacing of 1/48°. The model depth is >6000m at this location but only the upper 3000m are shown.

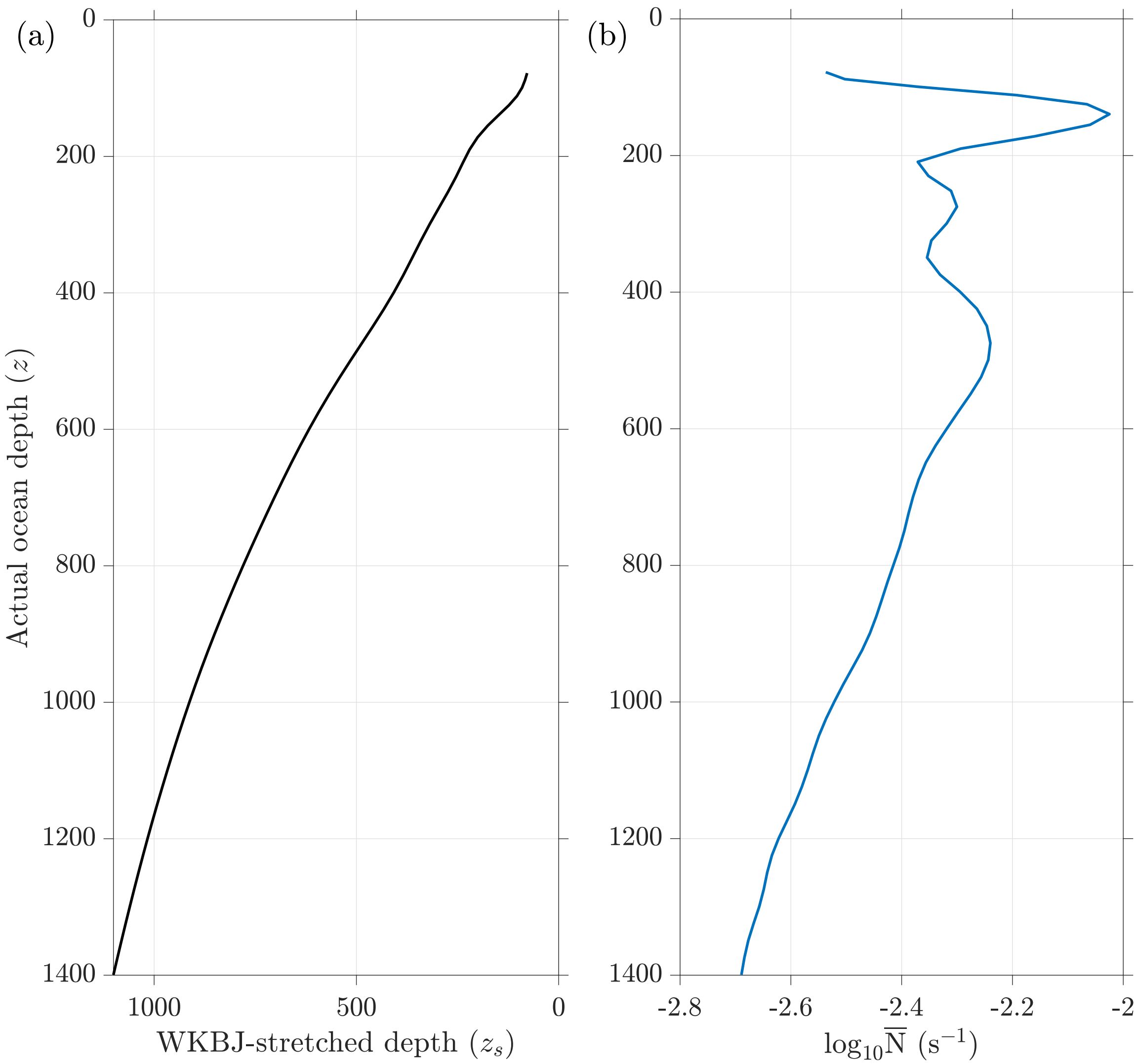

Figure S2. (a) WKBJ-stretched or buoyancy-frequency-stretched depth (z_s) is plotted against actual ocean depth (z) from the 264-level regional simulation at the MP4 location. Despite being from a different year, MP observations have a similar stretched depth vs. actual depth relationship at this location. All vertical wavenumbers calculated in this paper are based on stretched depths. (b) Vertical profile of the logarithm of the time-averaged buoyancy frequency $\overline{\mathrm{N}}(z)$ from the same simulation. Only 80–1400m of actual ocean depth from the simulation is shown here because all spectra in the main paper are calculated in this depth range.

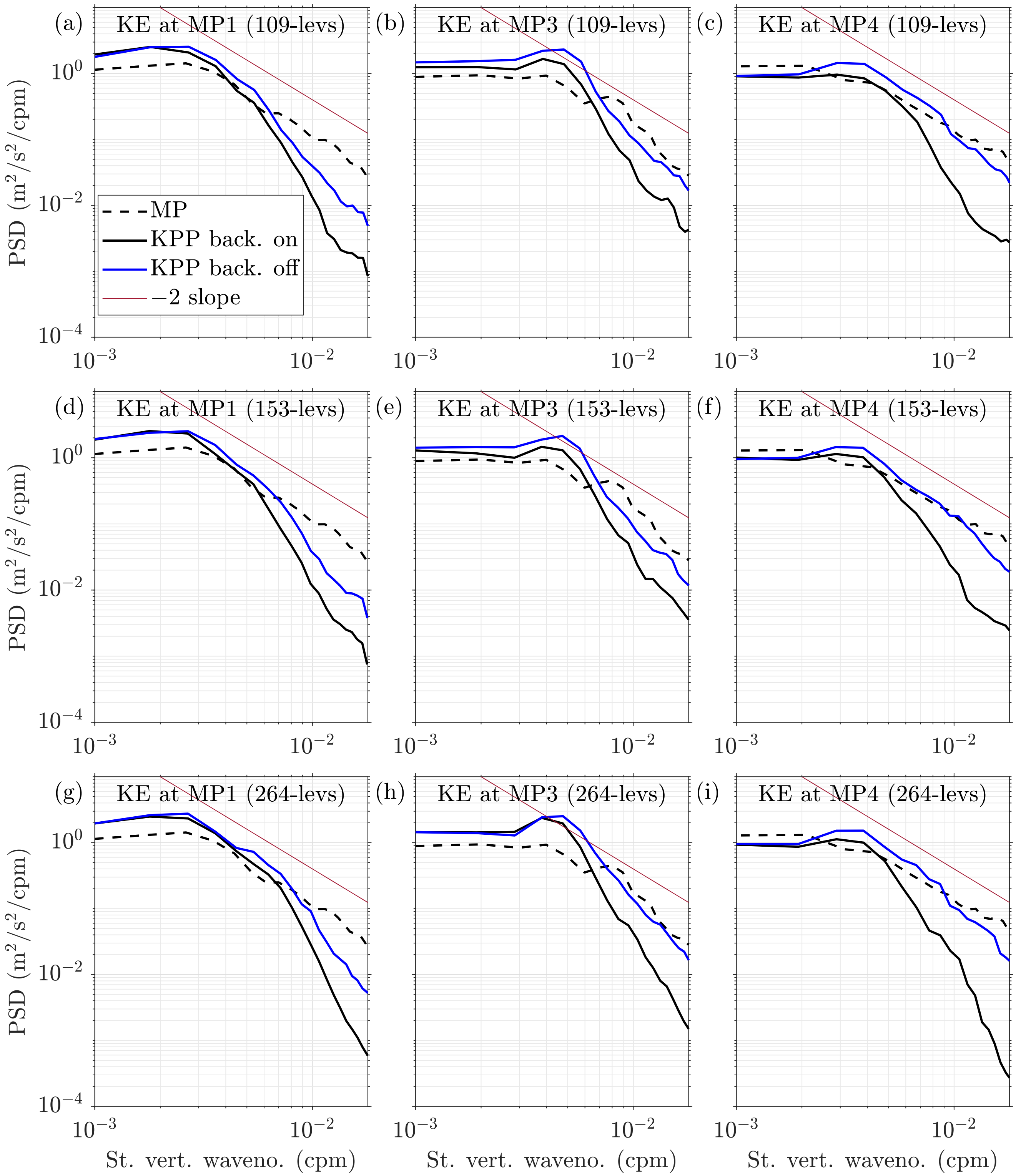

Figure S3. (Caption on next page)

Figure S3. (Previous page) Vertical wavenumber spectra of modeled KE (solid curves) for simulations with (a–c) 109 levels, (d–f) 153 levels, and (g–i) 264 levels, and with the background diffusivity and viscosity components of KPP turned on and off, at different locations as marked in Fig 1 (b) of the main paper are compared to observation (MP) KE spectra. The blue curves represent modeled KE spectra with the KPP background diffusivity and viscosity turned off, while the solid black curves represent modeled KE spectra with the KPP background viscosity set to $\mathcal{O}(10^{-4})$ m^{2}s^{-1} in the momentum equations and KPP background diffusivity set to $\mathcal{O}(10^{-7})$ m^{2}s^{-1} in the scalar equations which are also same as that of the global model. MP KE spectra are shown in black dashed curves in each. Modeled KE spectra are calculated in the depth range of 80–1400m while the MP KE spectra are calculated in the depth range of 85–1384m. The GM76 KE spectral slope of -2 is plotted in each for reference. The legends for all the subplots are in (a).

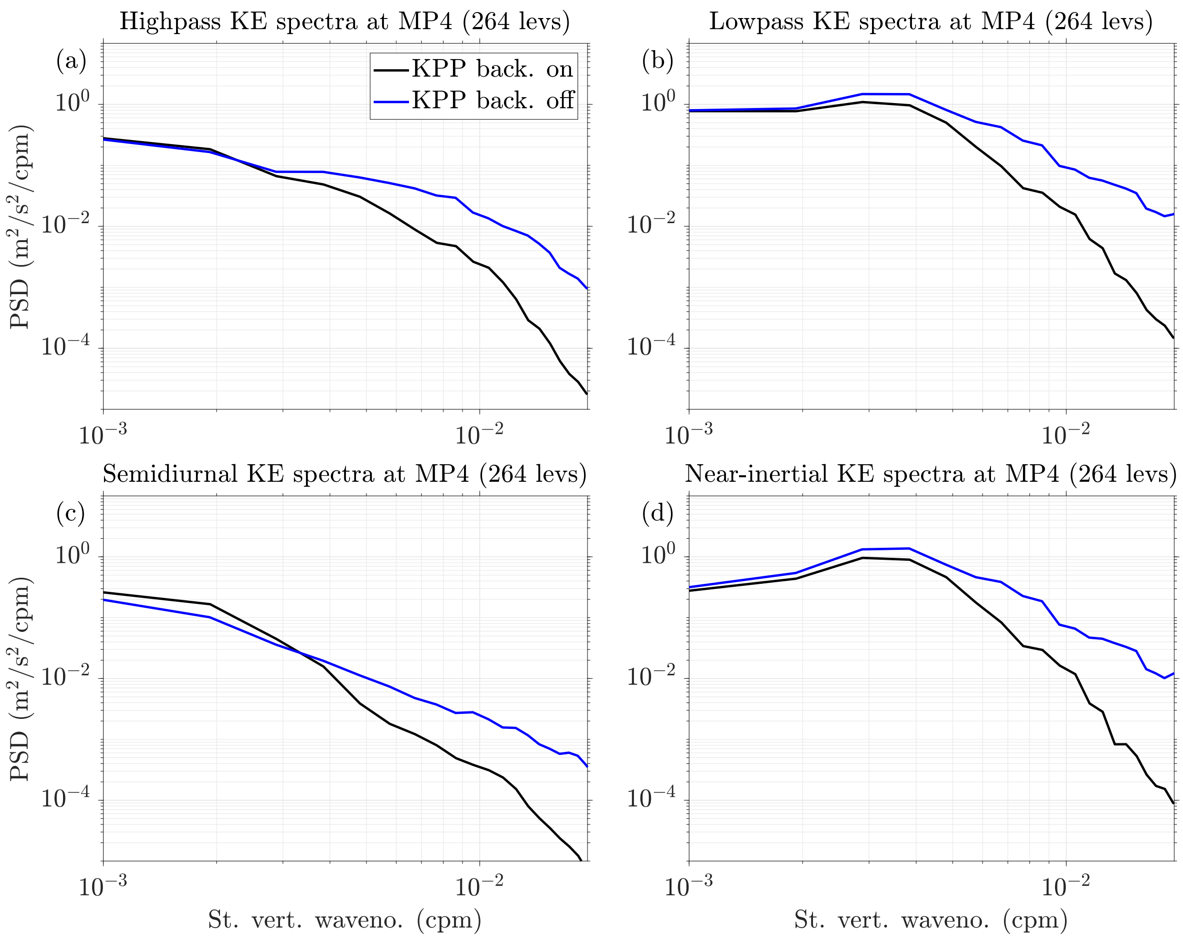

Figure S4. Effect of KPP background on the vertical wavenumber spectra of modeled KE at the MP4 location for the highest-resolution (264-level) simulation in the (a) high-pass or supertidal (>11.5 hr), (b) lowpass (<11.5 hr), (c) semidiurnal (11.5–13.5 hr), and (d) near-inertial (90–110% of 23.92 hr) frequency bands. These spectra are calculated in the depth range of 80–1400m. The modeled KE spectra with the KPP background turned off (blue curves) have increased high-wavenumber variance in all the frequency bands when compared to the KE spectra with the KPP background kept on (black curves).

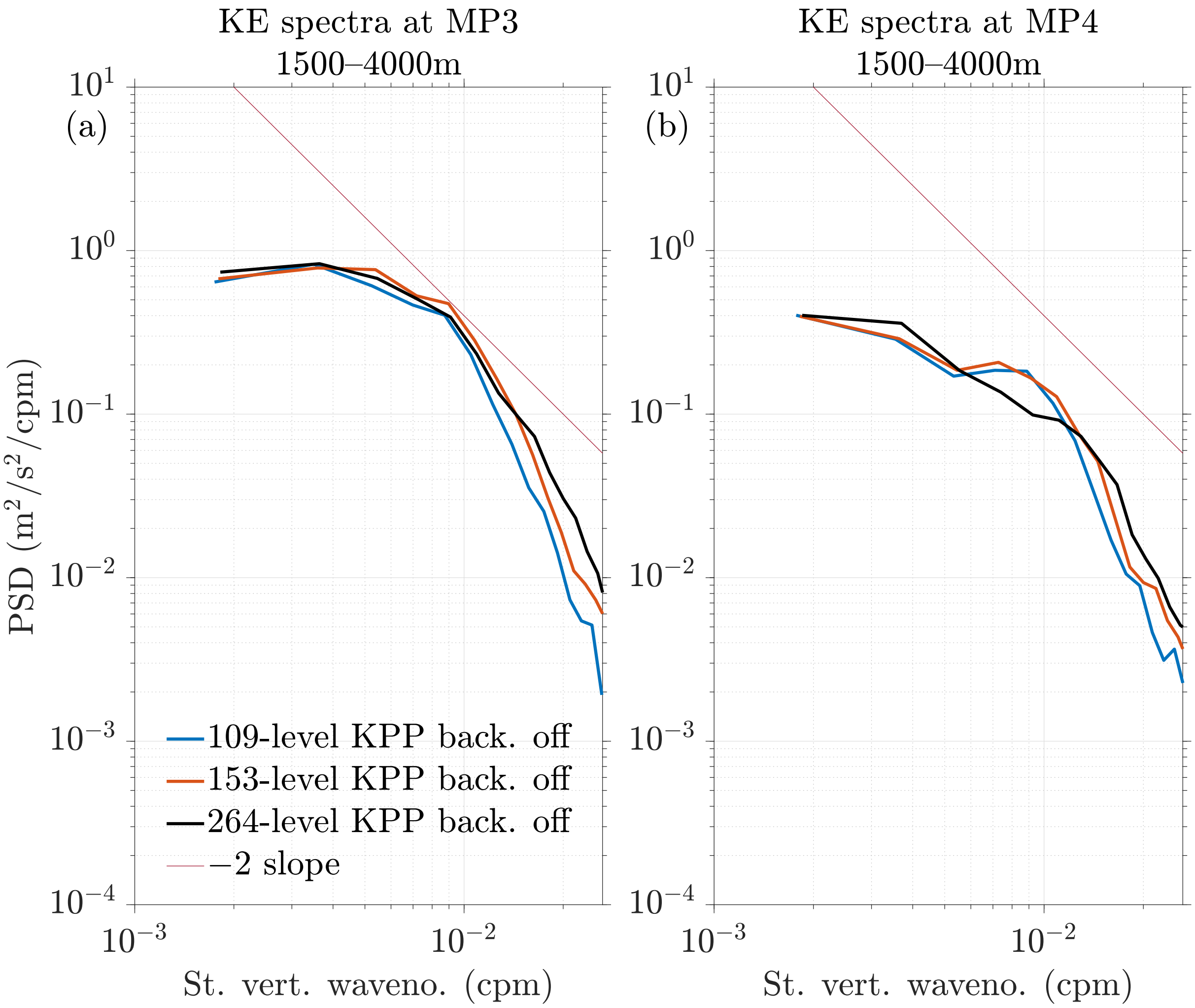

Figure S5. Vertical wavenumber spectra of modeled KE in the deep ocean (1500–4000m) demonstrate the improvement of the high-wavenumber internal wave continuum with an increase in model vertical resolution at (a) MP3 and (b) MP4 locations. There are no MP measurements in this depth range to compare the modeled spectra with observational spectra. The GM76 KE spectral slope of −2 is plotted in each for reference. The legends for both subplots are in (a).

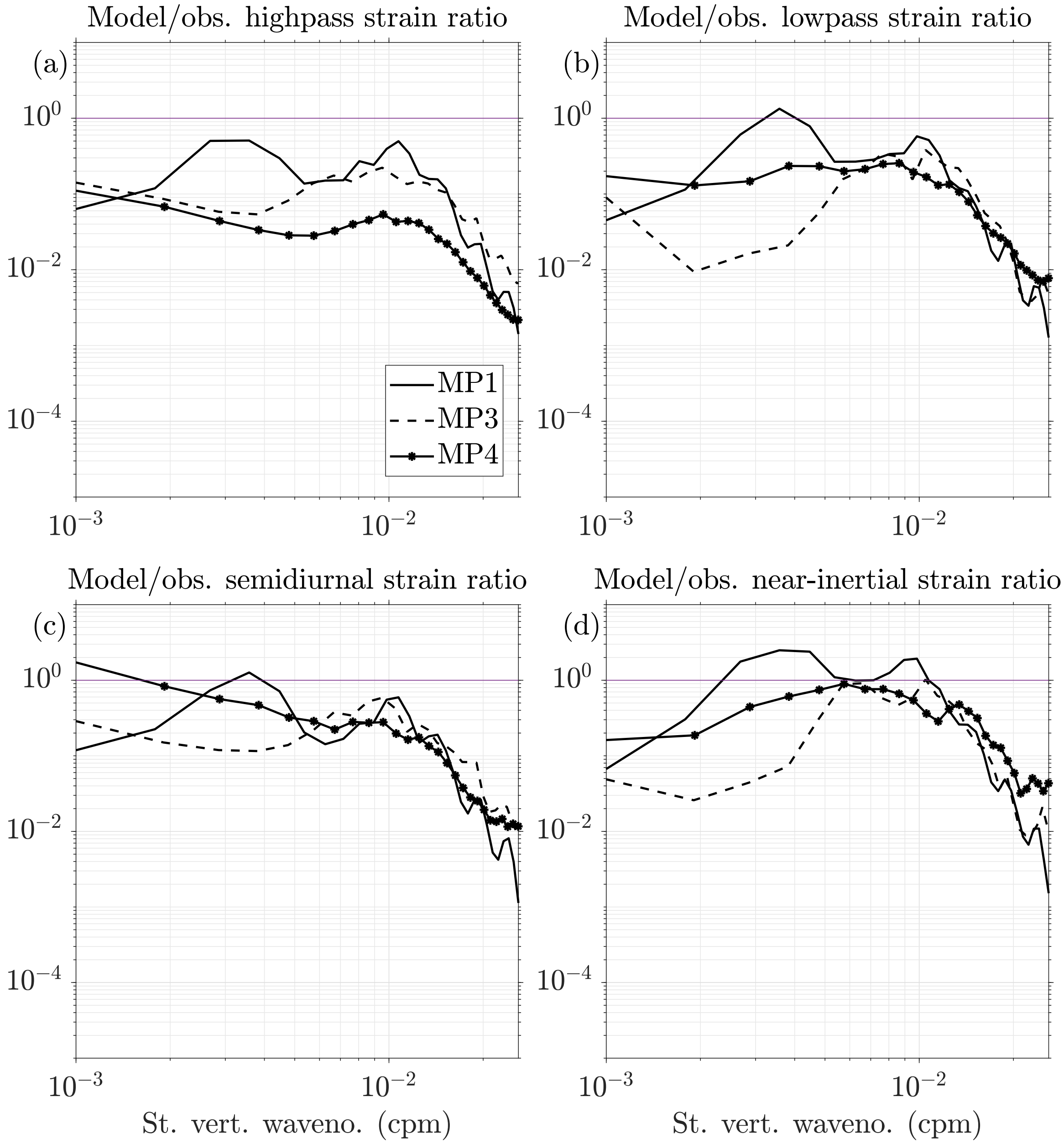

Figure S6. The ratio of strain $(\mathrm{N}^2 - \overline{\mathrm{N}^2})/\overline{\mathrm{N}^2}$ from the 264-level simulation in the depth range of 80–1400m with the KPP background turned off and from MP observations at MP1, MP3, and MP4 in different frequency bands as described in Fig S4. The legends for all the subplots are in (a). Extra horizontal lines are drawn at values of unity for reference.

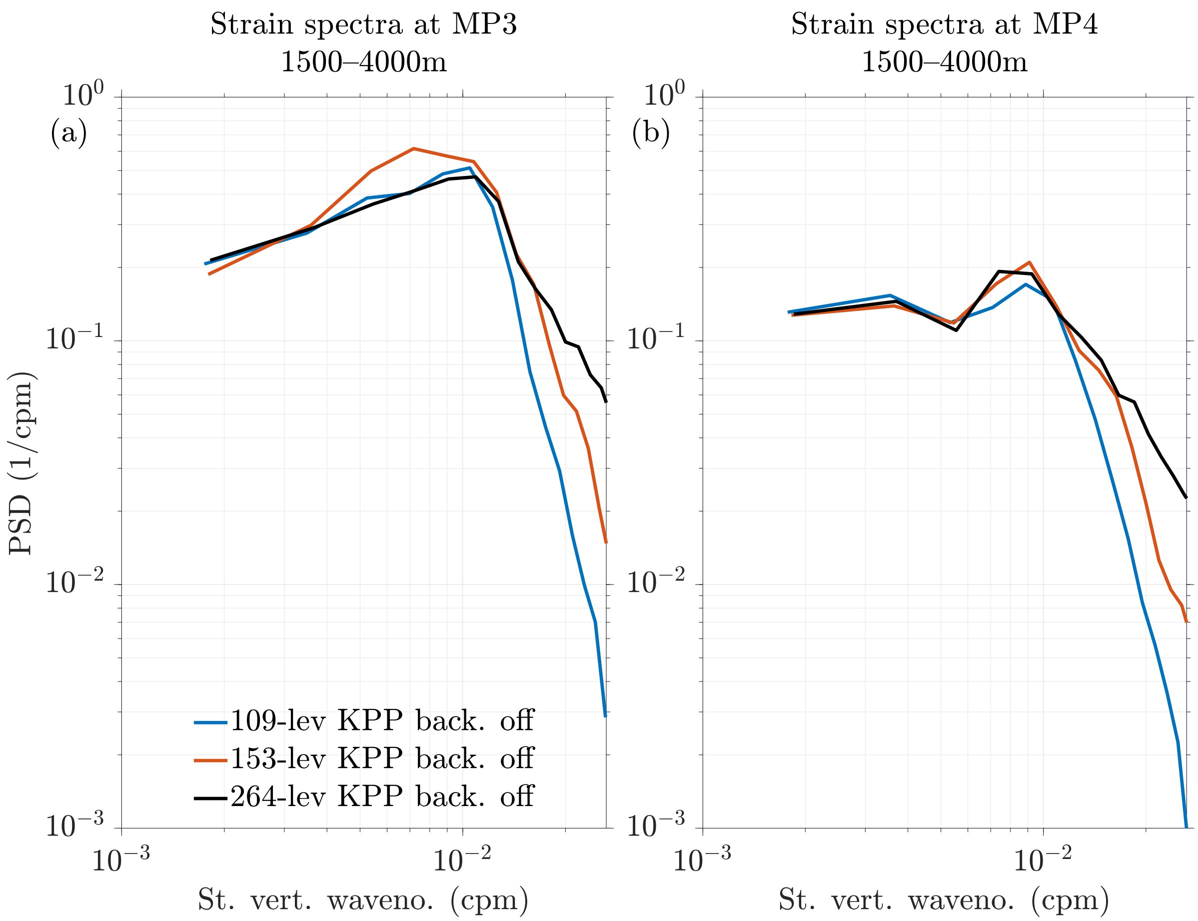

Figure S7. Vertical wavenumber spectra of modeled strain in the deep ocean (1500–4000m) demonstrate the improvement of strain variance in the internal wave continuum with an increase in model vertical resolution at (a) MP3 and (b) MP4 locations. All spectra are from simulations with the KPP background turned off. The legends for both subplots are in (a).

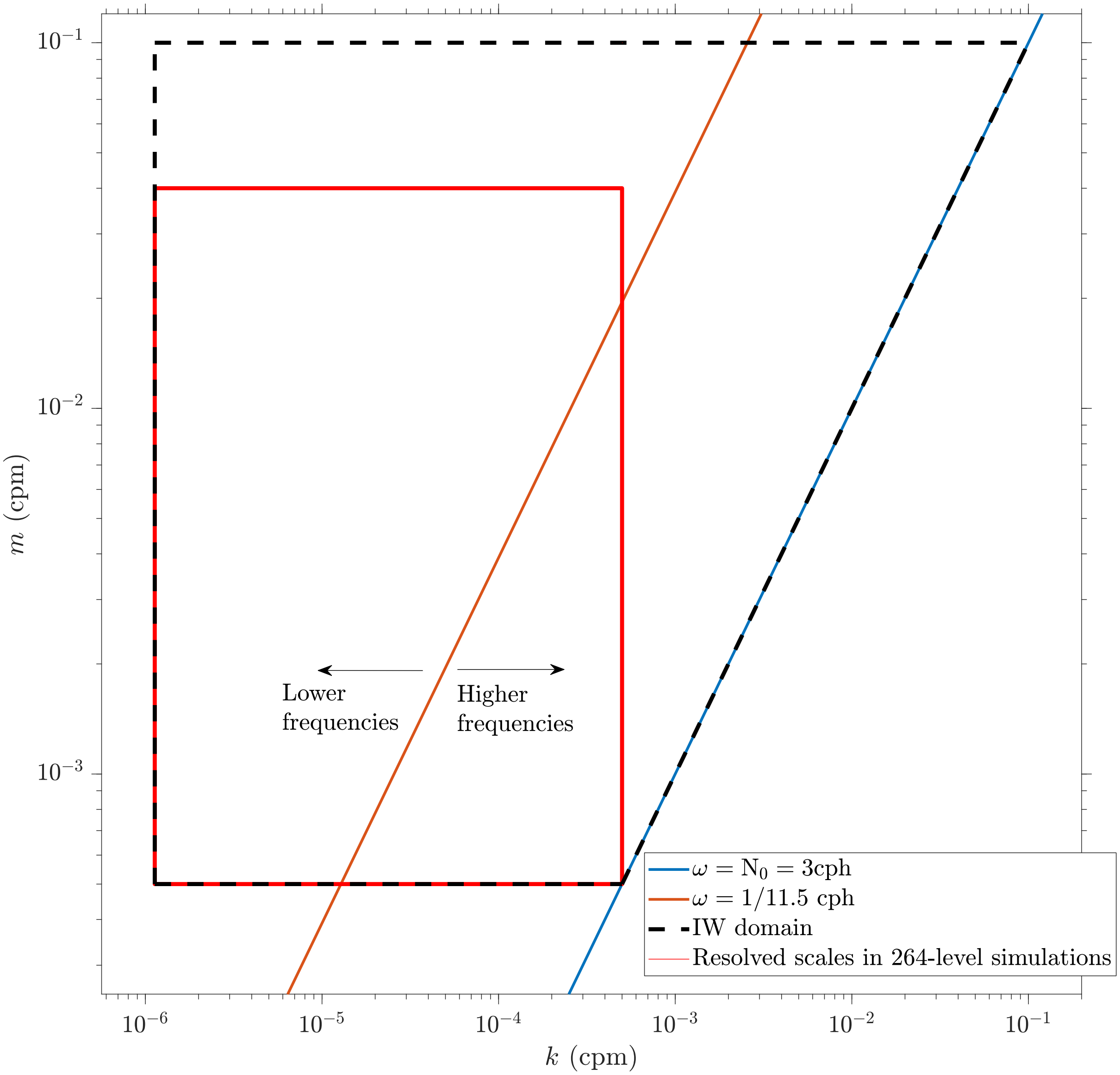

Figure S8. The approximate span of the ocean internal wave field is shown by the black dashed lines in a log-log plot of horizontal (k) and vertical (m) wavenumbers. The resolved internal wave scales in the 264-level simulation are bound by the red rectangle. The blue and orange lines are the internal wave dispersion relations at a constant frequency ω. The blue line is for $\omega = \mathrm{N}_0 = 3$ cph. The orange line is for $\omega = 1/11.5$ cph that demarcates the highpass (supertidal) and lowpass (subtidal) frequency bands. This figure is a variation of a diagram suggested by an anonymous reviewer.